

Cold streams in early massive hot haloes as the main mode of galaxy formation

A. Dekel¹, Y. Birnboim¹, G. Engel¹, J. Freundlich^{1,2}, T. Goerdt¹, M. Mumcuoglu¹, E. Neistein¹, C. Pichon³, R. Teyssier^{4,5}, & E. Zinger¹

¹Racah Institute of Physics, The Hebrew University, Jerusalem 91904, Israel

²Department de Physique, Ecole Normale Supérieure, 24 rue Lhomond, 75231 Paris cedex 05, France

³Institut d'Astrophysique de Paris and UPMC, 98bis Boulevard Arago, Paris 75014, France

⁴Institut de Recherches sur les lois Fondamentales de l'Univers, DSM, l'Orme des Merisiers, 91198 Gif-sur-Yvette, France

⁵Institute for Theoretical Physics, University of Zurich, CH-8057 Zurich, Switzerland

The massive galaxies in the young Universe, ten billion years ago, formed stars at surprising intensities.^{1,2} Although this is commonly attributed to violent mergers, the properties of many of these galaxies are incompatible with such events, showing gas-rich, clumpy, extended rotating disks not dominated by spheroids.^{1,3,4} Cosmological simulations⁵ and clustering theory^{6,7} are used to explore how these galaxies acquired their gas. Here we report that they are stream-fed galaxies, formed from steady, narrow, cold gas streams that penetrate the shock-heated media of massive dark matter haloes.^{8,9} A comparison with the observed abundance of star-forming galaxies implies that most of the input gas must rapidly convert to stars. One-third of the stream mass is in gas clumps leading to mergers of mass ratio greater than 1:10, and the rest is in smoother flows. With a merger duty cycle of 0.1, three-quarters of the galaxies forming stars at a given rate are fed by smooth streams. The rarer, submillimetre galaxies that form stars even more intensely^{2,10,11} are largely merger-induced starbursts. Unlike destructive mergers, the streams are likely to keep the rotating disk configuration intact, although turbulent and broken into giant star-forming clumps that merge into a central spheroid.^{12,13,4,14} This stream-driven scenario for the formation of disks and spheroids is an alternative to the merger picture.

Star-Formation Rate versus Halo Growth Rate

It appears that the most effective star formers in the Universe were galaxies of stellar and gas mass of $\sim 10^{11} M_{\odot}$ at redshifts $z = 2-3$, when the Universe was ~ 3 Gyr old. The common cases^{1,3} show star-formation rates (SFR) of $100-200 M_{\odot} \text{yr}^{-1}$. These include

UV-selected galaxies termed BX/BM¹⁵ and rest-frame optically selected galaxies termed sBzK,¹⁶ to be referred to collectively as “Star-Forming Galaxies” (SFGs). Their SFRs are much higher than the $4 M_{\odot} \text{yr}^{-1}$ in today’s Milky Way, while their masses and dynamical times are comparable. The comoving space density of SFGs is $n \simeq 2 \times 10^{-4} \text{Mpc}^{-3}$, implying within the standard cosmology (termed Λ CDM) that they reside in dark-matter haloes of masses $\lesssim 3.5 \times 10^{12} M_{\odot}$. The most extreme star formers are dusty Sub-Millimeter Galaxies (SMG),^{11,10} with SFRs of up to $\sim 1,000 M_{\odot} \text{yr}^{-1}$ and $n \simeq 2 \times 10^{-5} \text{Mpc}^{-3}$. Whereas most SMGs could be starbursts induced by major mergers, the kinematics of the SFGs indicate extended, clumpy, thick rotating disks that are incompatible with the expected compact or highly perturbed kinematics of ongoing mergers.^{3,1,17,4} The puzzle is how massive galaxies form most of their stars so efficiently at early times through a process other than a major merger. A necessary condition is a steady, rapid gas supply into massive disks.

It is first necessary to verify that the required rate of gas supply is compatible with the cosmological growth rate of dark matter haloes. The average growth rate of halo mass, M_v , through mergers and smooth accretion, is derived⁶ based on the EPS theory of gravitational clustering¹⁸ (Supplementary Information, SI, §1), or from cosmological simulations.^{19,20} For Λ CDM, the corresponding growth rate of the baryonic component is approximately

$$\dot{M} \simeq 6.6 M_{12}^{1.15} (1+z)^{2.25} f_{.165} M_{\odot} \text{yr}^{-1}, \quad (1)$$

where $M_{12} \equiv M_v/10^{12} M_{\odot}$, and $f_{.165}$ is the baryonic fraction in the haloes in units of the cosmological value, $f_b = 0.165$. Thus, at $z = 2.2$, the baryonic growth rate of haloes of $2 \times 10^{12} M_{\odot}$ is $\dot{M} \simeq 200 M_{\odot} \text{yr}^{-1}$, sufficient for fueling the SFR in SFGs. However, the margin by which this is sufficient is not large, implying that (1) the incoming material must be mostly gaseous, (2) the cold gas must efficiently penetrate into the inner halo, and (3) the SFR must closely follow the gas supply rate.

Penetrating Cold Narrow Streams

The deep penetration is not a trivial matter, given that the halo masses of $M_v > 10^{12} M_{\odot}$ are above the threshold for virial shock heating,^{21,22,9,8} $M_{\text{shock}} \lesssim 10^{12} M_{\odot}$. Such haloes are encompassed by a stable shock near their outer radius, R_v , inside which gravity and thermal energy are in virial equilibrium. Gas falling in through the shock is expected to heat up to the virial temperature and stall in quasi-static equilibrium before it cools and descends into the inner galaxy.²³ However, at $z \geq 2$, these hot haloes are penetrated by cold streams.^{9,8} Dekel & Birnboim⁸ pointed out that because early haloes with $M_v > M_{\text{shock}}$ populate the massive tail of the distribution, they are fed by dark-matter filaments from the cosmic web that are narrow compared to R_v and denser than the mean within the halo. The enhanced density of the gas along these filaments makes the flows along them unstoppable; in particular, they cool before they develop the pressure to support a shock, and thus avoid the shock heating (SI, §2).

To investigate the penetration of cold streams, we study the way gas feeds massive high- z galaxies in the cosmological MareNostrum simulation — an adaptive-mesh hydrodynamical

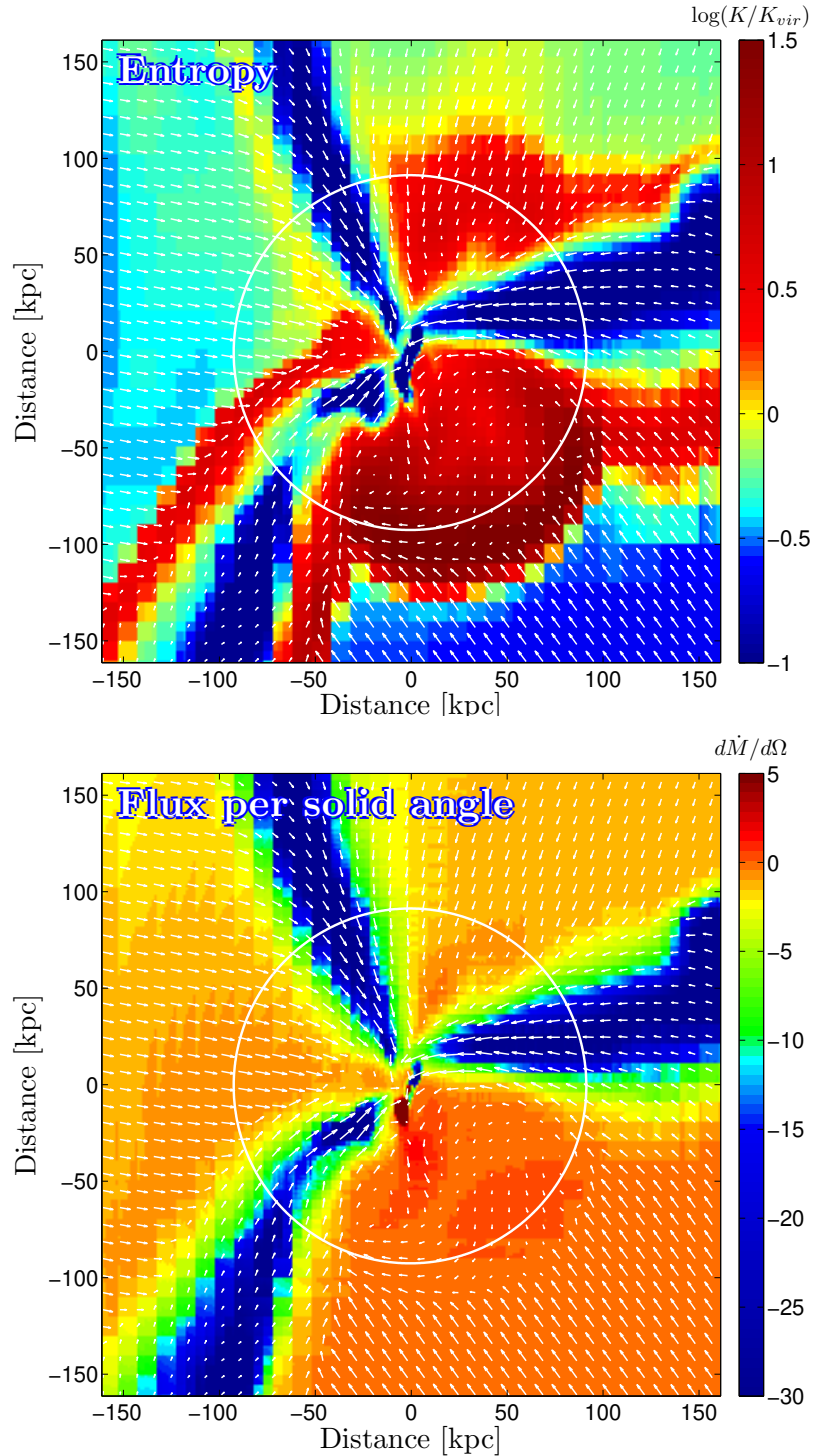


Figure 1. Entropy, velocity and inward flux of cold streams pouring through hot haloes. The maps refer to a thin slice through one of our fiducial galaxies of $M_v = 10^{12} M_\odot$ at $z = 2.5$. The arrows describe the velocity field, scaled such that the distance between the tails is 260 km s^{-1} . The circle marks the halo virial radius R_v . The **entropy**, $\log K = \log(T/\rho^{2/3})$, in units of the virial quantities, highlights (in red) the high-entropy medium filling the halo out to the virial shock outside R_v . It exhibits (in blue) three, radial, low-entropy streams that penetrate into the inner disk, seen edge-on. The radial **flux** per solid angle is $\dot{m} = r^2 \rho v_r$, in $M_\odot \text{ yr}^{-1} \text{ rad}^{-2}$, where ρ is the gas density and v_r the radial velocity.

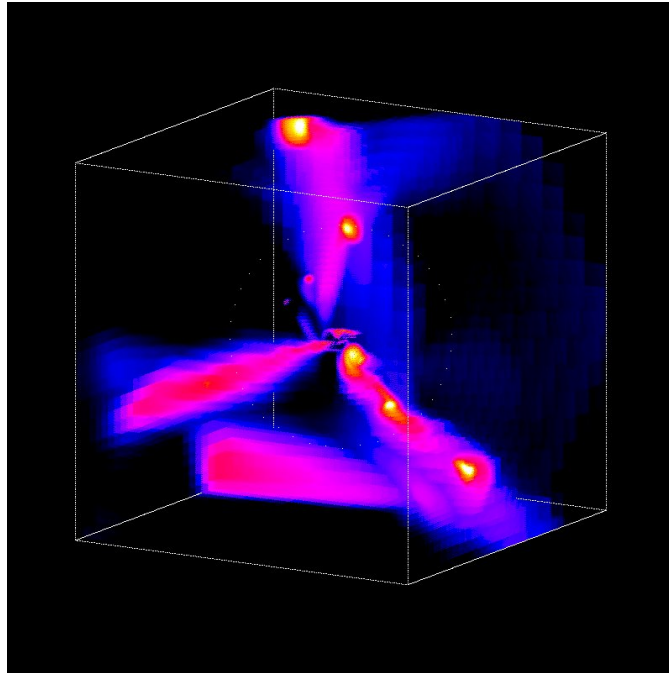


Figure 2. Streams in three dimensions. The map shows radial flux for the galaxy of Fig. 1 in a box of side length 320 kpc. The colours refer to inflow rate per solid angle of point-like tracers at the centers of cubic-grid cells. The dotted circle marks the halo virial radius. The appearance of three fairly radial streams seems to be generic in massive haloes at high redshift — a feature of the cosmic web that deserves an explanation. Two of the streams show gas clumps of mass on the order of one-tenth of the central galaxy, but most of the stream mass is smoother (SI, Fig. 10). The $\gtrsim 10^{10} M_{\odot}$ clumps, which involve about one-third of the incoming mass, are also gas rich — in the current simulation only 30% of their baryons turn into stars before they merge with the central galaxy.

simulation in a comoving box of side length 71 Mpc and a resolution of 1.4 kpc at the galaxy centers (SI §3). The gas maps in Figs. 1 & 2 demonstrate how the shock-heated, high-entropy, low-flux medium that fills most of the halo is penetrated by three narrow, high-flux streams of low-entropy gas (SI, Figs. 7-10). The flux map demonstrates that more than 90% of the inflow is channeled through the streams (blue), at a rate that remains roughly the same at all radii. This rate is several times higher than the spherical average outside the virial sphere, $\dot{m}_{\text{vir}} \simeq 8 M_{\odot} \text{yr}^{-1} \text{rad}^{-2}$ by eq. (4). The opening angle of a typical stream at R_{v} is $20^{\circ} - 30^{\circ}$, so the streams cover a total angular area of $\sim 0.4 \text{rad}^2$, namely a few percent of the sphere. When viewed from a given direction, the column density of cold gas below 10^5K is above 10^{20}cm^{-2} for 25% of the area within the virial radius. While the pictures show the inner disk, the disk width is not resolved, so the associated phenomena such as shocks, star formation and feedback are treated in an approximate way only.

The penetration is evaluated from the profiles of gas inflow rate, $\dot{M}(r)$, through shells

of radius r , Fig. 3 (SI, Fig. 11). The average profile reveals that the flow rate remains constant from well outside $R_v \sim 90$ kpc to the disk inside $r \sim 15$ kpc.

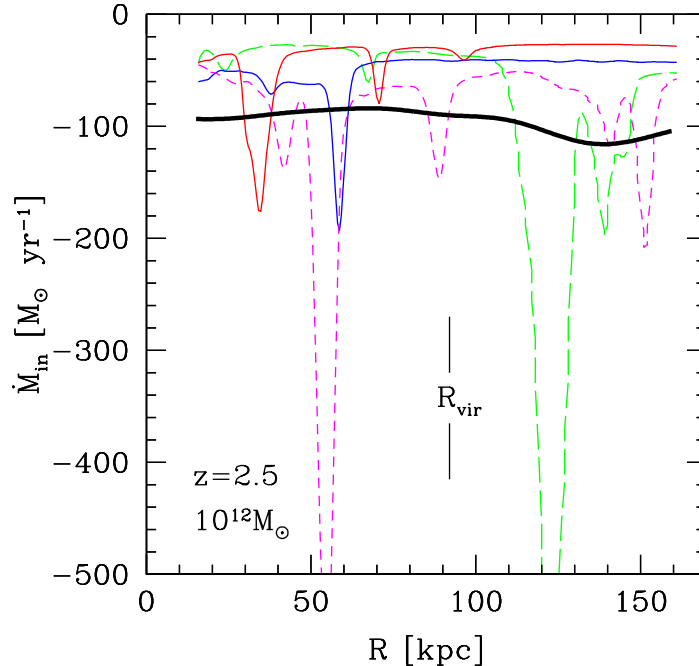


Figure 3. Accretion profiles $\dot{M}(r)$. Shown is the gas inflow rate through spherical shells of radius r , from the disk vicinity to almost twice the halo virial radius, obtained by integrating $r^2 \rho v_r$ over the whole shell. The thick black curve is the average over the simulated galaxies of the fiducial case, $M_v \simeq 10^{12} M_\odot$ at $z = 2.5$. It shows deep penetration at a roughly constant rate $\sim 100 M_\odot \text{ yr}^{-1}$, consistent with the virial growth rate predicted by eq. (4). Apparently, the inflow rate does decay while traveling through the halo, but this decay is roughly compensated by the higher cosmological inflow rate when that gas entered the halo, eq. (4), leading to the apparent constancy of accretion rate with radius. The coloured curves refer to four representative galaxies, two showing clumps with $\mu \gtrsim 0.1$ and two with smoother flows involving only mini-minor clumps of $\mu < 0.1$. Clumps with $\mu \gtrsim 0.3$ appear within $2R_v$ about once in ten galaxies; that is, major mergers are infrequent (SI, Fig. 11). The $\dot{M}(r)$ profiles serve for extracting the conditional probability distribution $P(\dot{M}|M_v)$, leading to the abundance $n(>\dot{M})$ (SI, Fig. 12).

Abundance of Gas Inflow Rates

To relate the feeding by streams to the observed abundance of galaxies as a function of SFR, we use the MareNostrum inflow-rate profiles to evaluate $n(>\dot{M})$, the comoving number density of galaxies with an inflow rate $>\dot{M}$. We first extract the conditional probability distribution $P(\dot{M}|M_v)$ by sampling the $\dot{M}(r)$ profiles uniformly in r , using the fact that the velocity along the streams is roughly constant (SI §§5,6). This is convolved with the halo mass function,²⁴ $n(M_v)$, to give

$$n(\dot{M}) = \int_0^\infty P(\dot{M}|M_v) n(M_v) dM_v . \quad (2)$$

The desired cumulative abundance $n(> \dot{M})$, obtained by integration over the inflow rates from \dot{M} to infinity, is shown at $z=2.2$ in Fig. 4. Assuming that the SFR equals \dot{M} , the curve referring to \dot{M} lies safely above the observed values, marked by the symbols, indicating that the gas input rate is sufficient to explain the SFR. However, \dot{M} and the SFR are allowed to differ only by a factor of ~ 2 , confirming our suspicion that the SFR must closely follow the gas-input rate. Because at $z \sim 2.2$ the star-forming galaxies constitute only a fraction of the observed $\sim 10^{11} M_{\odot}$ galaxies,^{25,26} the requirement for a SFR almost as great as \dot{M} , based on Fig. 4, becomes even stronger.

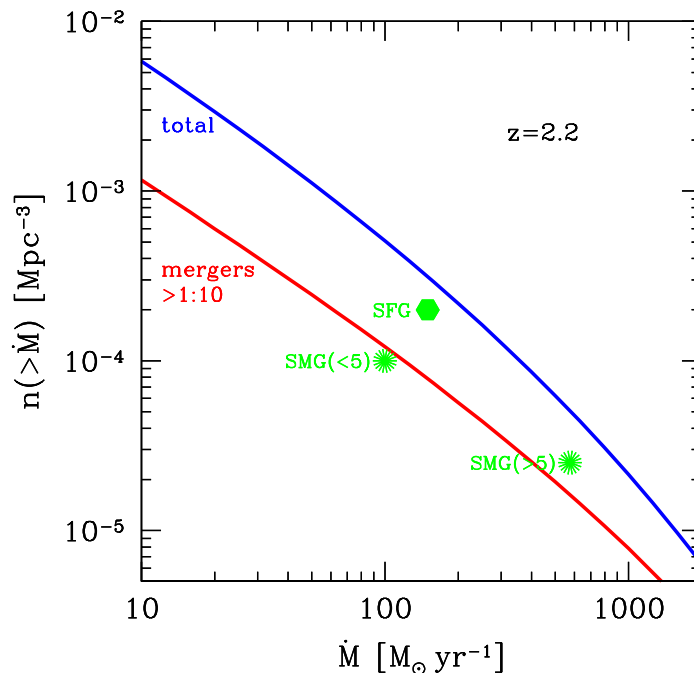


Figure 4. Abundance of galaxies as a function of gas inflow rate, $n(> \dot{M})$. Shown is the comoving number density, n , of galaxies with inflow rate higher than \dot{M} at $z=2.2$, as predicted from our analysis of the cosmological simulation. The upper curve refers to total inflow. It shows that galaxies with $\dot{M} > 150 M_{\odot} \text{ yr}^{-1}$ are expected at a comoving number density $n \sim 3 \times 10^{-4} \text{ Mpc}^{-3}$ (similar to estimates in other simulations^{27,28}). Fluxes as high as $\dot{M} > 500 M_{\odot} \text{ yr}^{-1}$ are anticipated at $n \sim 6 \times 10^{-5} \text{ Mpc}^{-3}$. The lower curve is similar, but limited to gas input by $\mu > 0.1$ mergers. The symbols represent the vicinity of where the observed massive star-forming galaxies can be located once their observed SFR is identified with \dot{M} . The sBzK/BX/BM galaxies are marked SFG.¹¹ The SMGs respectively brighter and fainter than 5 mJy are marked accordingly.^{11,10} We see that the overall gas inflow rate is sufficient for the observed SFR, but the small margin implies that the SFR must closely follow the rate of gas supply. Most of the massive star formers at a given SFR are expected to be observed while being fed by smooth flows rather than undergoing mergers. By studying the contribution of different halo masses to the abundance $n(> \dot{M})$, we learn that the high-SFR SFGs and SMGs are associated with haloes of mass $10^{12} - 10^{13} M_{\odot}$ (SI, Fig. 13).

Smooth Flows versus Mergers

By analysing the clumpiness of the gas streams, using the sharp peaks of inflow in the $\dot{M}(r)$ profiles, we address the role of mergers versus smooth flows. We evaluate each clump mass by integrating $M_{\text{clump}} = \int \dot{M}(r) dr/v_r(r)$ across the peak, and estimate a mass ratio for the expected merger by $\mu = M_{\text{clump}}/(f_b M_v)$, ignoring further mass loss in the clump on its way in and deviations of the galaxy baryon fraction from f_b . We use the term “merger” to describe any major or minor merger of $\mu \geq 0.1$, as distinct from “smooth” flows, which include “mini-minor” mergers with $\mu < 0.1$. We find that about one-third of the mass is flowing in as mergers and the rest as smoother flows. However, the central galaxy is fed by a clump of $\mu \geq 0.1$ during less than 10% of the time; that is, the duty cycle for mergers is $\eta \lesssim 0.1$. A similar estimate is obtained using EPS merger rates⁷ and starburst durations of ~ 50 Myr at $z=2.5$ from simulations²⁹ (SI, §5).

From the difference between the two curves of Fig. 4 we learn that only a quarter of the galaxies with a given \dot{M} are to be seen during a merger. The fact that the SFGs lie well above the merger curve even if the SFR is $\sim \dot{M}$ indicates that in most of them the star formation is driven by smooth streams. Thus, “SFG” could also stand for “Stream-Fed Galaxies”. This may explain why these galaxies maintain an extended, thick disk while doubling their mass over a halo crossing time.⁴ On the other hand, if the SFR is $\sim \dot{M}$, we learn from Fig. 4 that about half of the bright SMGs and most of the fainter SMGs lie below the merger curve and are therefore consistent with being merger-induced starbursts.¹¹

Conclusion and Discussion

We obtain that Stream-Fed Galaxies of baryonic mass $\sim 10^{11} M_\odot$ at $z \sim 2.5$ were the most productive star formers in the Universe. An integration of \dot{M} over halo mass and time reveals that most of the stars in the Universe were formed in Stream-Fed Galaxies, within haloes $> 2 \times 10^{11} M_\odot$ at $1.5 < z < 4$. The constraints on the overall SFR density at these epochs³⁰ imply that SFR has been suppressed in smaller galaxies, e.g., by photoionization and stellar feedback.^{31,32,8} The early presence of low-SFR galaxies^{25,26} requires quenching of SFR also at the massive end, perhaps due to gravitational heating by destructive streams.³³

The streams are likely also to be responsible for compact spheroids, as an alternative to mergers³⁴ and the associated heating by expanding shocks.^{23,33} Using eq. (4), we find that at $z \geq 2$ the streams can maintain both the high gas fraction and the turbulence necessary for the disk to breakup into giant clumps by gravitational instability, with dispersion-to-rotation ratio $\sigma/V \sim 0.25$, as observed.⁴ The clumps migrate inward and dissipatively merge into a spheroid.^{12,13} The stream carrying the largest coherent flux with an impact parameter of a few kiloparsecs determines the disk’s spin and orientation, and the stream clumps perturb it. The incoming clumps and the growing spheroid can eventually stabilize the disk and suppress star formation. We can thus associate the streams with the main mode of galaxy and star formation occurring in massive haloes at $z \sim 2-3$; the streams that create the disks also make them fragment into giant clumps that serve both as the

sites of efficient star formation and the progenitors of the central spheroid, which in turn helps the streams to quench star formation.

Although wet mergers may grow secondary disks³¹, they are not as frequent as the observed SFGs (Fig. 4), these disks are neither gas rich nor clumpy enough, and, unlike most SFGs, they are dominated by stellar spheroids.

The cold streams should be detectable by absorption or emission. For external background sources, our simulation predicts that haloes with $M_v \sim 10^{12} M_\odot$ at $z \sim 2.5$ should contain gas at temperature $< 10^5 \text{K}$ with column densities $> 10^{20} \text{cm}^{-2}$ covering $\sim 25\%$ of the area at radii between 20 and 100 kpc, with coherent velocities $\lesssim 200 \text{km s}^{-1}$. Sources at the central galaxies should show absorption by the radial streams in $\sim 5\%$ of the galaxies, flowing in at $\gtrsim 200 \text{km s}^{-1}$, with column densities $\sim 10^{21} \text{cm}^{-2}$ (SI, Figs. 7-9).

Received ; Accepted .

-
1. Genzel, R. *et al.* The rapid formation of a large rotating disk galaxy three billion years after the Big Bang. *Nature* **442**, 786–789 (2006).
 2. Chapman, S. C., Smail, I., Blain, A. W. & Ivison, R. J. A Population of Hot, Dusty Ultraluminous Galaxies at $z \sim 2$. *Astrophys. J.* **614**, 671–678 (2004).
 3. Förster Schreiber, N. M. *et al.* SINFONI Integral Field Spectroscopy of $z \sim 2$ UV-selected Galaxies: Rotation Curves and Dynamical Evolution. *Astrophys. J.* **645**, 1062–1075 (2006).
 4. Genzel, R. *et al.* From rings to bulges: evidence for rapid secular galaxy evolution at $z \sim 2$ from integral field spectroscopy in the SINS survey. ArXiv e-prints 0807.1184 (2008).
 5. Ocvirk, P., Pichon, C. & Teyssier, R. Bimodal gas accretion in the MareNostrum galaxy formation simulation. ArXiv e-prints 0803.4506 (2008).
 6. Neistein, E., van den Bosch, F. C. & Dekel, A. Natural downsizing in hierarchical galaxy formation. *Mon. Not. R. Astron. Soc.* **372**, 933–948 (2006).
 7. Neistein, E. & Dekel, A. Merger Rates of Dark-Matter Haloes. ArXiv e-prints 0802.0198 (2008).
 8. Dekel, A. & Birnboim, Y. Galaxy bimodality due to cold flows and shock heating. *Mon. Not. R. Astron. Soc.* **368**, 2–20 (2006).
 9. Kereš, D., Katz, N., Weinberg, D. H. & Davé, R. How do galaxies get their gas? *Mon. Not. R. Astron. Soc.* **363**, 2–28 (2005).
 10. Wall, J. V., Pope, A. & Scott, D. The evolution of submillimetre galaxies: two populations and a redshift cut-off. *Mon. Not. R. Astron. Soc.* **383**, 435–444 (2008).
 11. Tacconi, L. J. *et al.* Submillimeter Galaxies at $z \sim 2$: Evidence for Major Mergers and Constraints on Lifetimes, IMF, and CO-H₂ Conversion Factor. *Astrophys. J.* **680**, 246–262 (2008).

12. Noguchi, M. Early Evolution of Disk Galaxies: Formation of Bulges in Clumpy Young Galactic Disks. *Astrophys. J.* **514**, 77–95 (1999).
13. Elmegreen, B., Bournaud, F. & Elmegreen, D. M. Bulge Formation by the Coalescence of Giant Clumps in Primordial Disk Galaxies. (2008).
14. Dekel, A., Sari, R. & Ceverino, D. Formation of Massive Galaxies at High Redshift: Cold Streams, Clumpy Disks and Compact Spheroids. ArXiv e-prints 0901.2458 (2009).
15. Adelberger, K. L. *et al.* Optical Selection of Star-forming Galaxies at Redshifts $1 < z < 3$. *Astrophys. J.* **607**, 226–240 (2004).
16. Daddi, E. *et al.* A New Photometric Technique for the Joint Selection of Star-forming and Passive Galaxies at $1.4 < z < 2.5$. *Astrophys. J.* **617**, 746–764 (2004).
17. Bouché, N. *et al.* Dynamical Properties of $z \sim 2$ Star-forming Galaxies and a Universal Star Formation Relation. *Astrophys. J.* **671**, 303–309 (2007).
18. Lacey, C. & Cole, S. Merger rates in hierarchical models of galaxy formation. *Mon. Not. R. Astron. Soc.* **262**, 627–649 (1993).
19. Neistein, E. & Dekel, A. Constructing merger trees that mimic N-body simulations. *Mon. Not. R. Astron. Soc.* **383**, 615–626 (2008).
20. Genel, S. *et al.* Mergers and Mass Accretion Rates in Galaxy Assembly: The Millennium Simulation Compared to Observations of $z \sim 2$ Galaxies. (2008).
21. Birnboim, Y. & Dekel, A. Virial shocks in galactic haloes? *Mon. Not. R. Astron. Soc.* **345**, 349–364 (2003).
22. Binney, J. On the origin of the galaxy luminosity function. *Mon. Not. R. Astron. Soc.* **347**, 1093–1096 (2004).
23. Birnboim, Y., Dekel, A. & Neistein, E. Bursting and quenching in massive galaxies without major mergers or AGNs. *Mon. Not. R. Astron. Soc.* **380**, 339–352 (2007).
24. Sheth, R. K. & Tormen, G. An excursion set model of hierarchical clustering: ellipsoidal collapse and the moving barrier. *Mon. Not. R. Astron. Soc.* **329**, 61–75 (2002).
25. Kriek, M. *et al.* Spectroscopic Identification of Massive Galaxies at $z \sim 2.3$ with Strongly Suppressed Star Formation. *Astrophys. J. Lett.* **649**, L71–L74 (2006).
26. van Dokkum, P. G. *et al.* Confirmation of the Remarkable Compactness of Massive Quiescent Galaxies at $z \sim 2.3$: Early-Type Galaxies Did not Form in a Simple Monolithic Collapse. *Astrophys. J. Lett.* **677**, L5–L8 (2008).
27. Finlator, K., Davé, R., Papovich, C. & Hernquist, L. The Physical and Photometric Properties of High-Redshift Galaxies in Cosmological Hydrodynamic Simulations. *Astrophys. J.* **639**, 672–694 (2006).
28. Nagamine, K., Ouchi, M., Springel, V. & Hernquist, L. Lyman-alpha Emitters and Lyman-break Galaxies at $z=3-6$ in Cosmological SPH Simulations. ArXiv e-prints 0802.0228 (2008).

29. Cox, T. J., Jonsson, P., Somerville, R. S., Primack, J. R. & Dekel, A. The effect of galaxy mass ratio on merger-driven starbursts. *Mon. Not. R. Astron. Soc.* **384**, 386–409 (2008).
30. Hopkins, A. M. On the Evolution of Star-forming Galaxies. *Astrophys. J.* **615**, 209–221 (2004).
31. Dekel, A. & Silk, J. The origin of dwarf galaxies, cold dark matter, and biased galaxy formation. *Astrophys. J.* **303**, 39–55 (1986).
32. Dekel, A. & Woo, J. Feedback and the fundamental line of low-luminosity low-surface-brightness/dwarf galaxies. *Mon. Not. R. Astron. Soc.* **344**, 1131–1144 (2003).
33. Dekel, A. & Birnboim, Y. Gravitational quenching in massive galaxies and clusters by clumpy accretion. *Mon. Not. R. Astron. Soc.* **383**, 119–138 (2008).
34. Robertson, B. E. & Bullock, J. S. High-Redshift Galaxy Kinematics: Constraints on Models of Disk Formation. ArXiv e-prints 0808.1100 (2008).
35. Komatsu, E. *et al.* Five-Year Wilkinson Microwave Anisotropy Probe (WMAP) Observations: Cosmological Interpretation. ArXiv e-prints 0803.0547 (2008).
36. Press, W. H. & Schechter, P. Formation of Galaxies and Clusters of Galaxies by Self-Similar Gravitational Condensation. *Astrophys. J.* **187**, 425–438 (1974).
37. Springel, V. *et al.* Simulations of the formation, evolution and clustering of galaxies and quasars. *Nature* **435**, 629–636 (2005).
38. Cattaneo, A., Dekel, A., Devriendt, J., Guiderdoni, B. & Blaizot, J. Modelling the galaxy bimodality: shutdown above a critical halo mass. *Mon. Not. R. Astron. Soc.* **370**, 1651–1665 (2006).
39. Croton, D. J. *et al.* The many lives of active galactic nuclei: cooling flows, black holes and the luminosities and colours of galaxies. *Mon. Not. R. Astron. Soc.* **365**, 11–28 (2006).
40. Bower, R. G. *et al.* Breaking the hierarchy of galaxy formation. *Mon. Not. R. Astron. Soc.* **370**, 645–655 (2006).
41. Cattaneo, A., Dekel, A., Faber, S. M. & Guiderdoni, B. *et al.* Downsizing by Shutdown in Red Galaxies. ArXiv e-prints 0801.1673 (2008).
42. Prunet, S. *et al.* Initial Conditions for Large Cosmological Simulations. ArXiv e-prints 0804.3536 (2008).
43. Teyssier, R. Cosmological hydrodynamics with adaptive mesh refinement. A new high resolution code called RAMSES. *Astron. Astrophys.* **385**, 337–364 (2002).
44. Rasera, Y. & Teyssier, R. The history of the baryon budget. Cosmic logistics in a hierarchical universe. *Astron. Astrophys.* **445**, 1–27 (2006).

Acknowledgments We acknowledge stimulating discussions with N. Bouche, S.M. Faber, R. Genzel, D. Koo, A. Kravtsov, A. Pope, J.R. Primack, J. Prochaska, A. Sternberg &

J. Wall. This research has been supported by the France-Israel Teamwork in Sciences, the German-Israel Science Foundation, the Israel Science Foundation, a NASA Theory Program at UCSC, and a Minerva fellowship (TG). We thank the computer resources and technical support by the Barcelona Centro Nacional de Supercomputacion. The simulation is part of the Horizon collaboration.

Author Information Correspondence and requests for materials should be addressed to A.D. (dekel@phys.huji.ac.il).

SUPPLEMENTARY INFORMATION

This is an extension of the Letter to Nature, aimed at providing further details, in support of the results reported in the main body of the Letter.

1 Halo growth by EPS

Neistein et al.⁶ used the EPS¹⁸ theory of cosmological clustering into spherical haloes in virial equilibrium to derive a robust approximation for the average growth rate of halo virial mass M_v ,

$$d \ln M_v / d\omega = -(2/\pi)^{1/2} [\sigma^2(M_v/q) - \sigma^2(M_v)]^{-1/2}, \quad \omega \equiv \delta_c / D(t). \quad (3)$$

The time variable ω , which makes the expression time invariant, is inversely proportional to $D(t)$, the linear growth rate of density fluctuations at time t in the assumed cosmology, with $\delta_c \simeq 1.68$. The power spectrum of initial density fluctuations enters via the variance $\sigma^2(M_v)$. The constant q is 2.2 with an uncertainty of ± 0.1 intrinsic to the EPS theory. Eq. (3) has been confirmed to resemble the assembly rate in cosmological N -body simulations.¹⁹

For the Λ CDM cosmology,³⁵ a flat Universe with 72% dark energy, mass dominated by cold dark matter, and fluctuation normalization parameter $\sigma_8 = 0.8$, the corresponding growth rate of the baryonic component is well fitted by the practical formula⁶

$$\dot{M} \simeq 6.6 M_{12}^{1.15} (1+z)^{2.25} f_{.165} M_\odot \text{ yr}^{-1}, \quad (4)$$

where $M_{12} \equiv M_v / 10^{12} M_\odot$, and $f_{.165}$ is the baryonic fraction in the matter assembled into haloes in units of the cosmological value $f_b = 0.165$.

2 On the origin of narrow streams

Dekel & Birnboim 2006⁸ (hereafter DB06), following the simulations by Keres et al. (2005, §6.2) and their own analysis of the simulations by A. Kravtsov, pointed out that at redshifts higher than $z_{\text{crit}} \sim 2$, narrow cold streams penetrate deep into the dark-matter haloes even when the haloes are more massive than the shock-heating scale, $M_{\text{shock}} \lesssim 10^{12} M_\odot$, and proposed a possible explanation for this phenomenon. This prediction is summarized in Fig. 5.

The critical condition for a stable virial shock is that the radiative cooling rate behind the shock is slower than the compression rate, $t_{\text{cool}}^{-1} < t_{\text{comp}}^{-1}$, allowing the buildup of pressure support behind the shock against global gravitational collapse.²¹ Based on a spherical analysis, DB06 found that a virial shock should exist in dark-matter haloes above a threshold mass $M_{\text{shock}} \lesssim 10^{12} M_\odot$ that is rather constant in time, at an actual value that is sensitive to the metallicity of the gas in the halo. The existence of such a threshold mass and its value as a function of redshift have been confirmed by the analysis of cosmological simulations.^{9,8,23,5} However, at high redshifts, even above the threshold mass, a shock is not

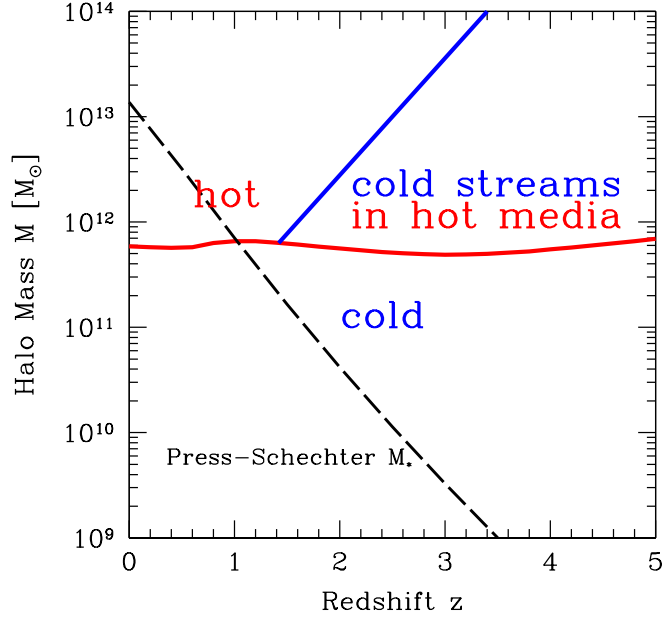


Figure 5. Analytic prediction for the regimes dominated by cold flows and shock-heated medium in the plane of halo mass and redshift, based on Fig. 7 of DB06. The nearly horizontal curve marks the robust threshold mass for a stable shock based on spherical infall analysis, $M_{\text{shock}}(z)$. Below this curve the flows are predicted to be predominantly cold and above it a shock-heated medium is expected to extend out to the halo virial radius. The inclined solid curve is the conjectured upper limit for cold streams, valid at redshifts higher than $z_{\text{crit}} \sim 2$. The hot medium in haloes of $M_v > M_{\text{shock}}$ at $z > z_{\text{crit}}$ is predicted to host penetrating cold streams, while haloes of a similar mass at $z < z_{\text{crit}}$ are expected to be all hot, shutting off most of the gas supply to the inner galaxy. Also shown is the characteristic Press-Schechter halo mass $M_*(z)$; it is much smaller than M_{shock} at $z > 2$.

expected to develop along narrow, cold, radial streams that penetrate through the halo, because the cooling there is more efficient than in the surrounding halo.

The appearance of intense streams at high z , as opposed to their absence at low z , is likely to reflect the interplay between the shock-heating scale and the independent characteristic scale of nonlinear clustering, i.e., the Press-Schechter³⁶ mass M_* that corresponds to the typical dark-matter haloes forming at a given epoch. The key difference between the two epochs is that the rapid growth of M_* with time, as seen in Fig. 5, makes $M_{\text{shock}} \gg M_*$ at $z > 2$ while $M_{\text{shock}} \sim M_*$ at lower redshifts.

Cosmological N -body simulations^{9,37} reveal that while the rare dark-matter haloes of $M_v \gg M_*$ tend to form at the nodes of intersection of a few filaments of the cosmic web, the typical haloes of $M_v \sim M_*$ tend to reside inside such filaments. Since the filament width is comparable to the typical halo size $R_* \propto M_*^{1/3}$ and seems not to vary much with position along the filament, one expects the rare haloes to be fed by a few streams that are narrow

compared to the halo size, while the typical haloes accrete from a wide angle in a practically spherical pattern. Assuming that at any given epoch the accretion rate of dark matter, \dot{M} , is roughly proportional to the halo mass M_v (Eq. 1 of the Letter), while the virial densities in haloes of all masses are the same (by definition), the geometrical difference implies that the densities in the filaments penetrating $M_v \gg M_*$ haloes are higher by a factor of a few than the typical densities in their host haloes. The above is demonstrated in Fig. 6 (as well as in Fig. 5 of Ocvirk, Pichon & Teyssier 2008).

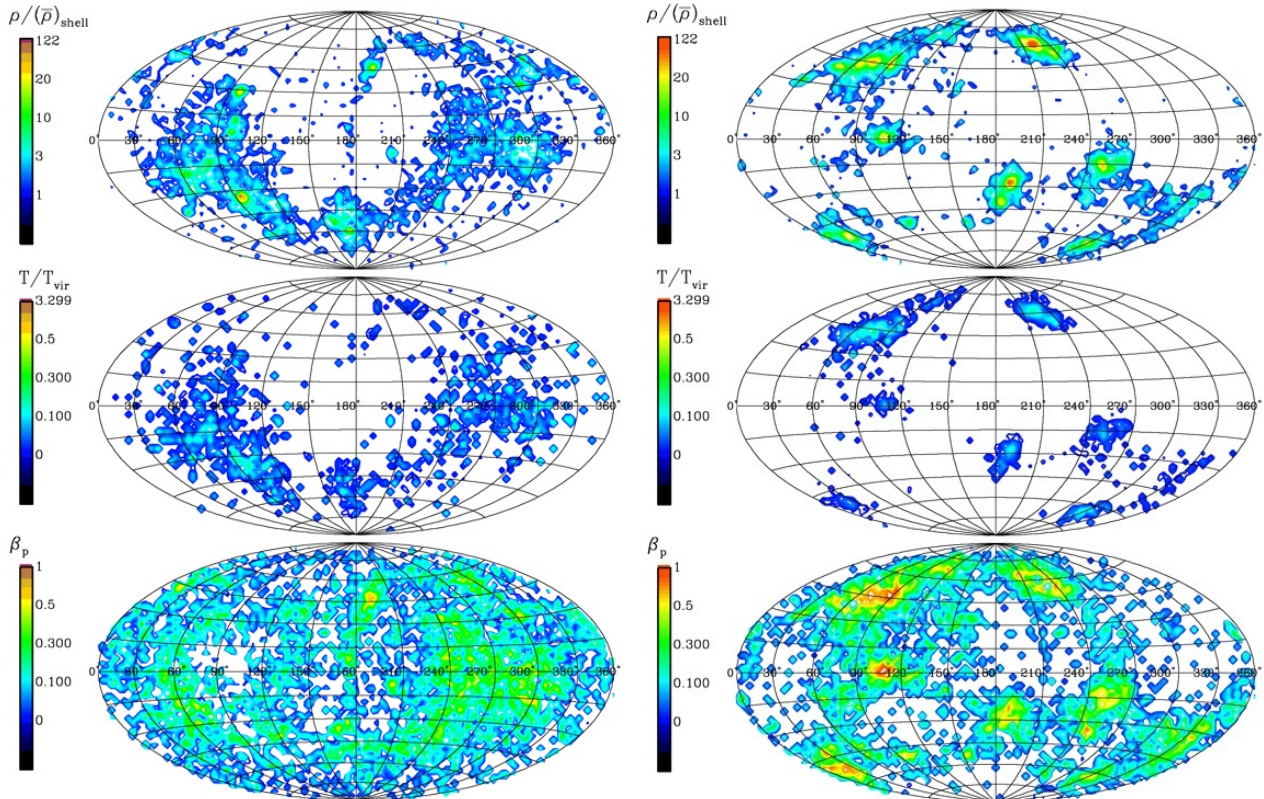


Figure 6. The pattern of dark-matter inflow in a shell $(1-3)R_v$ outside two sample haloes from a cosmological N-body simulation at $z = 0$ (based on P. Seleson & A. Dekel, in preparation). **Left:** a typical halo with $M_v \sim M_*$. **Right:** a rare halo with $M_v \gg M_*$. In terms of the different ways by which these two haloes are fed by dark-matter, they correspond to two haloes of the same mass $M_v \sim 10^{12}M_\odot$, but at $z \sim 0$ and $z \sim 2 - 3$ respectively. **Top:** dark-matter density contrast about the mean density in the shell. **Middle:** particle velocity dispersion (loosely termed “temperature”), in terms of the virial value. **Bottom:** infall velocity, represented by the anisotropy parameter β , where $\beta = 0$ corresponds to isotropic velocities and $\beta = 1$ to pure radial motions. We see that the typical halo resides inside a broad filament so it is practically fed by wide-angle diffuse accretion. On the other hand, the rare halo is fed by narrow, dense, radially in-flowing filaments.

Assuming that the density of the gas flowing along the filaments scales with the dark-matter density, and that the infall velocity is comparable to the halo virial velocity, one

expects the cooling rate in the filaments feeding an $M_v \gg M_*$ halo to be higher by a factor of a few than in the surrounding spherical halo. If the compression rate in the filaments is comparable to that in the host halo, this implies that the thin filaments should have a harder time supporting a stable shock. As a result, the critical halo mass for shock heating in the filaments feeding it must be larger by a factor of a few. This is the case for $M_v \gtrsim M_{\text{shock}}$ haloes at high redshifts.

A crude estimate along the lines above led DB06 to the conjectured upper limit for penetrating streams shown in Fig. 5:

$$M_{\text{stream}} \sim \frac{M_{\text{shock}}}{fM_*} M_{\text{shock}} \quad \text{for} \quad fM_* < M_{\text{shock}} , \quad (5)$$

where the characteristic width of the streams is $\propto (fM_*)^{1/3}$, with f a factor of order a few. At low z , where $fM_* > M_{\text{shock}}$, cold flows exist only for $M_v < M_{\text{shock}}$. At high z , where $fM_* < M_{\text{shock}}$, cold streams appear even in $M_v > M_{\text{shock}}$ haloes where shocks have heated part of the gas, as long as $M_v < M_{\text{stream}}$. The critical redshift z_{crit} separating these two regimes is defined by

$$fM_*(z_{\text{crit}}) = M_{\text{shock}} . \quad (6)$$

This crude maximum mass for cold streams is shown in Fig. 5 for an arbitrary choice of $f = 3$.

A preliminary analysis of the MareNostrum simulation⁵ confirms the crude prediction of eq. (5), when taking into account the lower metallicities in the simulation compared to that assumed in the analytic calculation. The streams analysed in the current Letter, in dark-matter haloes of $M_v = 10^{12} M_\odot$ at $z = 2.5$, represent an encouraging confirmation of the validity of the DB06 conjecture. Further analysis in progress (T. Goerdt et al., in preparation) indicates, for example, that at $z = 2.5$, the fraction of inflow in cold streams drops by a factor of three at $M_v \simeq 2 \times 10^{13} M_\odot$, much in the spirit of the crude prediction of Fig. 5. The permitted cold gas supply by streams in massive haloes at high redshift, followed by a shutdown above M_{shock} at low redshifts, turn out to provide good match to many observed galaxy properties when these features are incorporated in semi-analytic simulations of galaxy formation.^{38–41} Still, the dependence of the stream properties on redshift and halo mass is yet to be explored in a more quantitative way.

3 The MareNostrum simulation

The cosmological simulation^{5,42} used in the present analysis has been performed with the Eulerian AMR code RAMSES⁴³ on 2,048 processors of the MareNostrum supercomputer. The code simulates the coupled gas and dark-matter dynamics, using a Particle-Mesh scheme for the dark-matter component and a second-order Godunov scheme for the gas component. In order to describe the formation of dense star-forming disks, the code includes metal-dependent radiative cooling, UV heating by a standard photo-ionizing background, star formation, supernovae feedback and metal enrichment. The simulation box of co-moving $50 h^{-1} \text{Mpc}$ involved $1,024^3$ dark-matter h particles and 4×10^9 gas cells. Using a

quasi-Lagrangian refinement strategy, the spatial resolution reaches $\sim 1 h^{-1} \text{kpc}$ in physical units at all times. The dark-matter particle mass is $\sim 10^7 M_\odot$, so each of the haloes studied here consists of $\sim 10^5$ particles within the virial radius. Since one can reliably describe the formation of haloes down to ~ 100 particles,⁴⁴ namely $\sim 10^9 M_\odot$, the $10^{12} M_\odot$ haloes addressed here are three orders of magnitude above the minimum halo mass. This simulation allows us to capture the important properties of gas accretion into galaxies in more than 100 haloes of $\sim 10^{12} M_\odot$ at $z \sim 2.5$, thus providing a large statistical sample. A first analysis of galaxies from this simulation⁵ have confirmed the bi-modal nature of cold flows and hot media as a function of mass and redshift.⁸

Our current analysis is based on robust features that are properly simulated, such as the large-scale structure of the streams, the total flux in them, and the gas clumps larger than $10^9 M_\odot$. However, the finite resolution does not allow a fair treatment of small-scale gas phenomena such as turbulence in the hot gas, ram-pressure stripping of clumps, hydrodynamical instabilities at the stream boundaries, and the formation of small clumps. Furthermore, the current resolution does not allow a detailed study of the disks that form at the halo centers as the disk thickness is barely resolved. More accurate analysis of the fine stream structure and disk buildup should await simulations of higher resolution.

4 Maps of entropy, flux and density

Figs. 7 to 9 extend the visual information provided by Figs. 1 and 2 of the Letter. They display different gas properties that highlight the structure and kinematics of the cold streams in three simulated galaxies of $M_v = 10^{12} M_\odot$ at $z = 2.5$.

The entropy maps show $\log(T/\rho^{2/3})$ where the temperature and gas density are in units of the virial temperature and mean density within the halo virial radius R_v . They exhibit the virial shock, covering most of the area of the virial sphere and sometimes extending beyond $2R_v$. The narrow streams are of much lower entropy, by more than three orders of magnitude, comparable to the low entropy in the central disk they lead to. The boundaries between the streams and the hot medium within the virial radius are sharp and well defined. We also note that semi-cylindrical shocks sometimes partly surround the elongated streams long before they enter the halo virial radius.

The arrows mark the velocity field projected on the slice plane, and the flux colour maps show the flow rate per solid angle, $\dot{m} = r^2 \rho v_r$. The flux inward is almost exclusively channeled through the narrow streams, typically involving 95% of the total inflow rate. This flux is several times the average over a sphere, $\dot{m}_{\text{vir}} \simeq 8 M_\odot \text{yr}^{-1} \text{rad}^{-2}$. The opening angle of a typical stream at R_v is $20 - 30^\circ$, so the streams cover a total area of $\sim 0.4 \text{rad}^2$, namely a few percent of the sphere. The velocity field in the hot medium is turbulent and sometimes showing vast outflows. The inward flux over most of the sphere area is negligible, both inside and outside the virial radius or the virial shock. The streaming velocities are supersonic, with a Mach number of order a few.

Although the streams tend to be rather radial when viewed on scales comparable to the halo virial radius, some of them flow in with impact parameters on the order of 10 kpc,

comparable to the disk sizes. The steady high flux along a line of a rather fixed orientation with a non-negligible impact parameter is the source of angular momentum required for the buildup of an extended rotating disk (A. Zinger et al., in preparation).

The gas density maps emphasize the narrowness of the streams, and reveal that they are typically denser than the surrounding medium by more than an order of magnitude. This confirms the prediction described in §2, and explains why a virial shock is avoided along the streams, allowing them to penetrate cold and unperturbed into the inner halo.

The column-density maps of the in-flowing material are obtained by summing up the densities in grid cells along each line of sight inside the box of side 320 kpc. The cells that enter this sum are only those where the inward flux per solid angle is at least twice the average over a sphere based on Eq. 1 of the Letter. These maps highlight the three-dimensional configuration of radial streams, and the clumps along some of them. Such column density maps will serve us in producing detailed predictions to guide observations in search of the cold streams in high-redshift galaxies, in absorption and in emission.

Fig. 10 displays three-dimensional TIPSYP* pictures of the radial influx \dot{m} , similar to Fig. 2 of the Letter. It shows the overall structure of the in-flowing streams in 3D perspective for four simulated haloes. The pictures reveal that the typical configuration is of three major narrow streams. Some of the streams are straight lines, and others are curved. Some of the streams are of rather fixed width from well outside R_v , and others display a conical shape, starting broad at large radii and getting narrower as they penetrate into the halo. The gas streams show dense clumps, with about one third of the stream mass in clumps of mass ratio $\mu > 0.1$, namely mass above $\sim 10^{10} M_\odot$. The rest is in smaller clumps, some clearly hidden below the resolution limit. Since these mini-minor clumps are not expected to cause significant damage to the central disk,²⁹ we can refer to them in this respect as “smooth” flows. It is not clear at this point to what extent the smooth component is truly smooth or built by mini-minor clumps, and whether the perfect smoothness has a physical origin or is merely a numerical artifact, but this distinction does not make a qualitative difference to our present discussion.

*<http://www-hpcc.astro.washington.edu/tools/tipsy/tipsy.html>

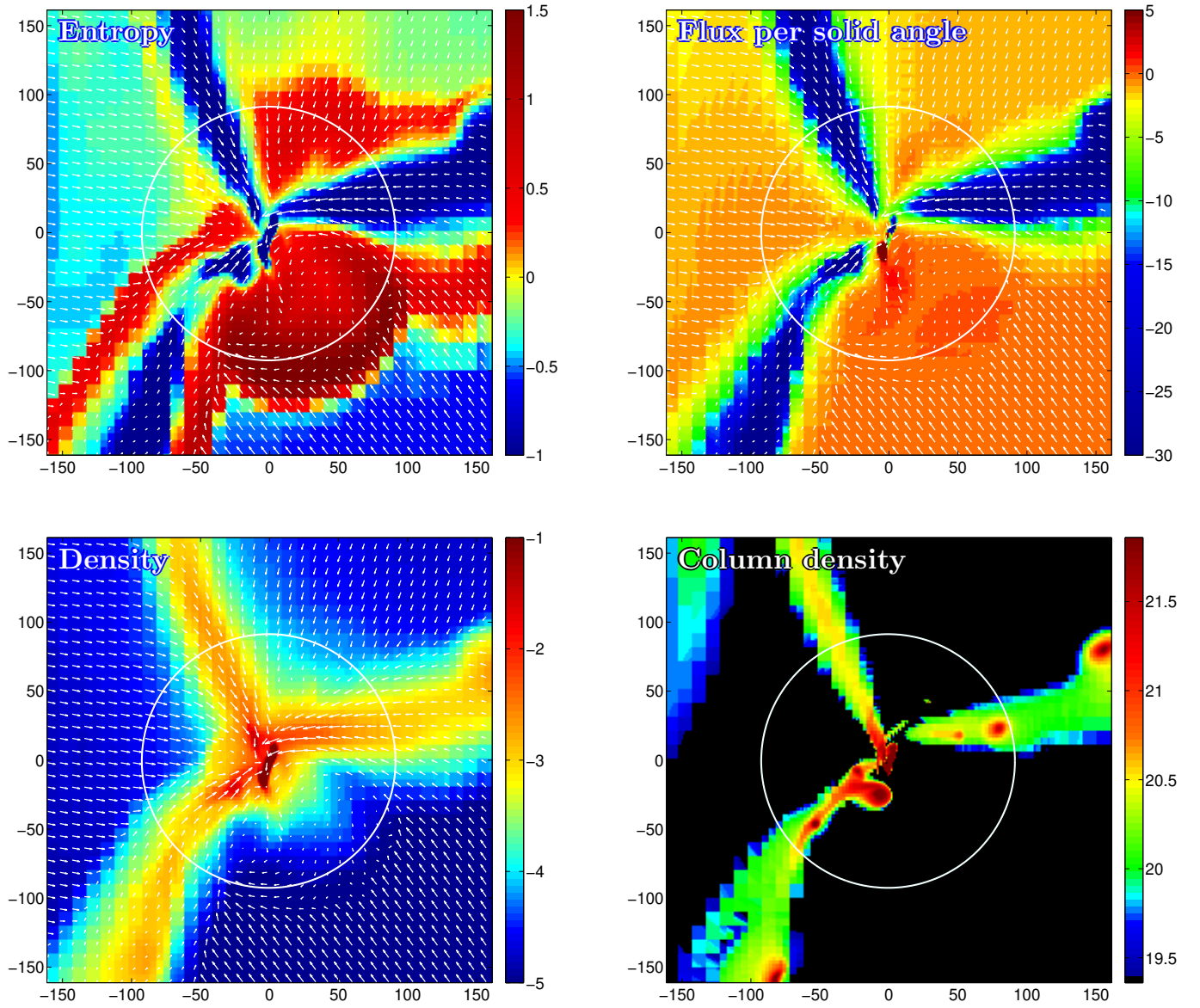


Figure 7. Gas in halo 314 of the MareNostrum simulation. Three maps refer to a thin equatorial slice. They show (a) entropy $\log K = \log(T/\rho^{2/3})$ in units of the virial quantities, (b) radial flux $\dot{m} = r^2 \rho v_r$ in $M_\odot \text{ yr}^{-1} \text{ rad}^{-2}$, and (c) \log density in atoms per cm^{-3} . The fourth panel shows \log column density through the 3D box of side 320 kpc, in cm^{-2} , considering only the cells where the radial flux inward is at least twice as high as the average over a shell based on Eq. 1 of the Letter. The circle marks the virial radius.

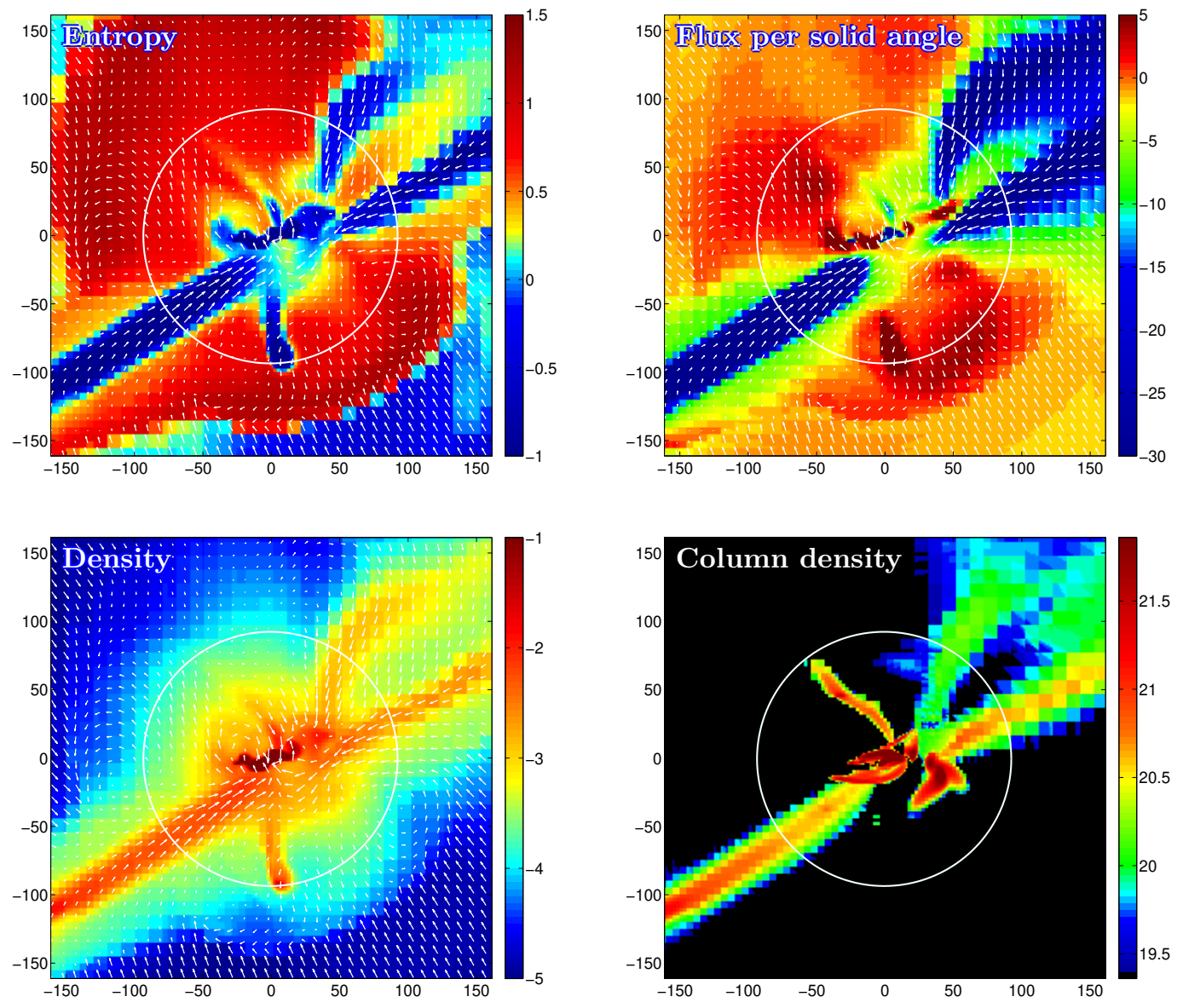


Figure 8. Gas in halo 303 of the MareNostrum simulation. See Fig. 7.

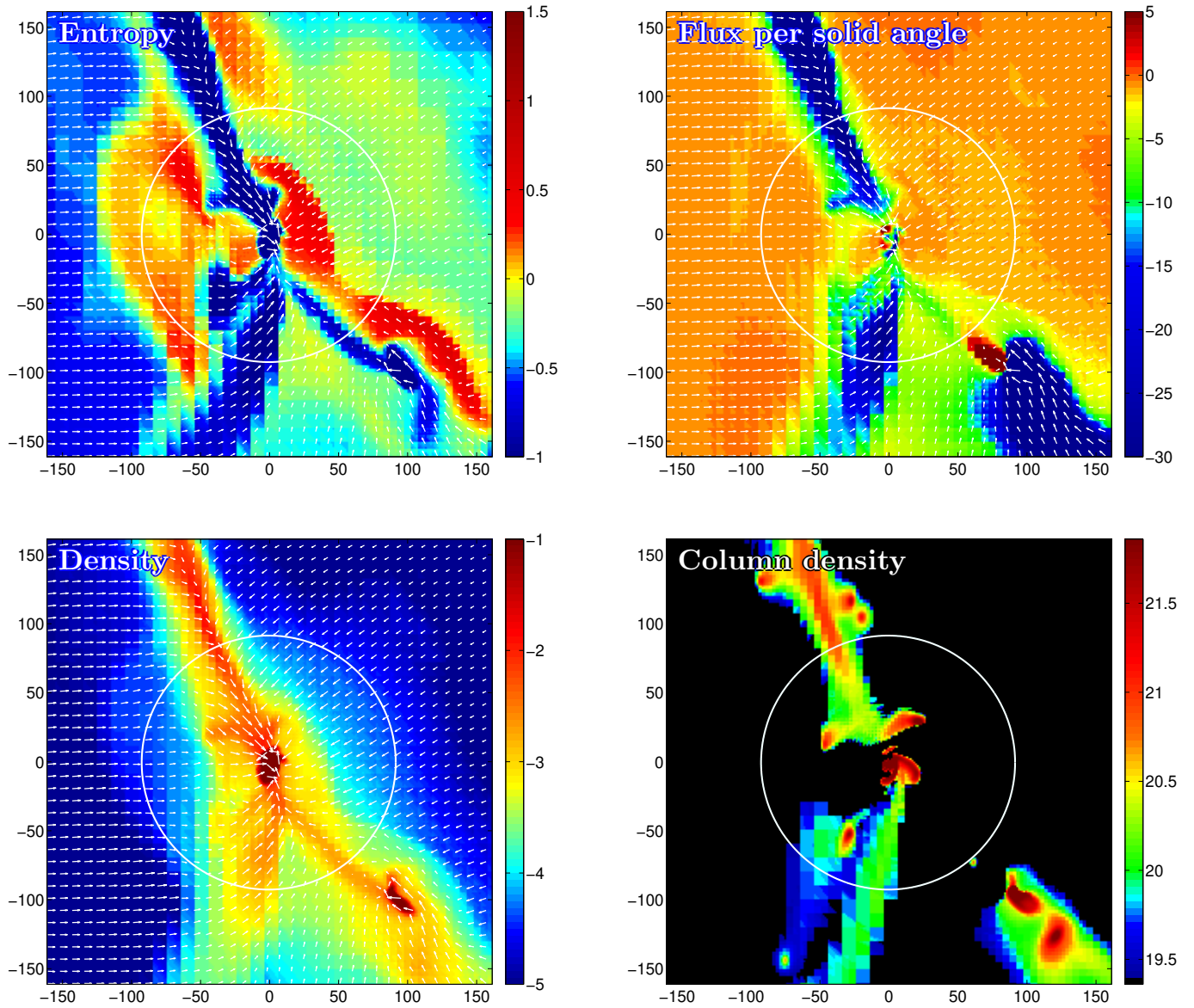


Figure 9. Gas in halo 311 of the MareNostrum simulation. See Fig. 7.

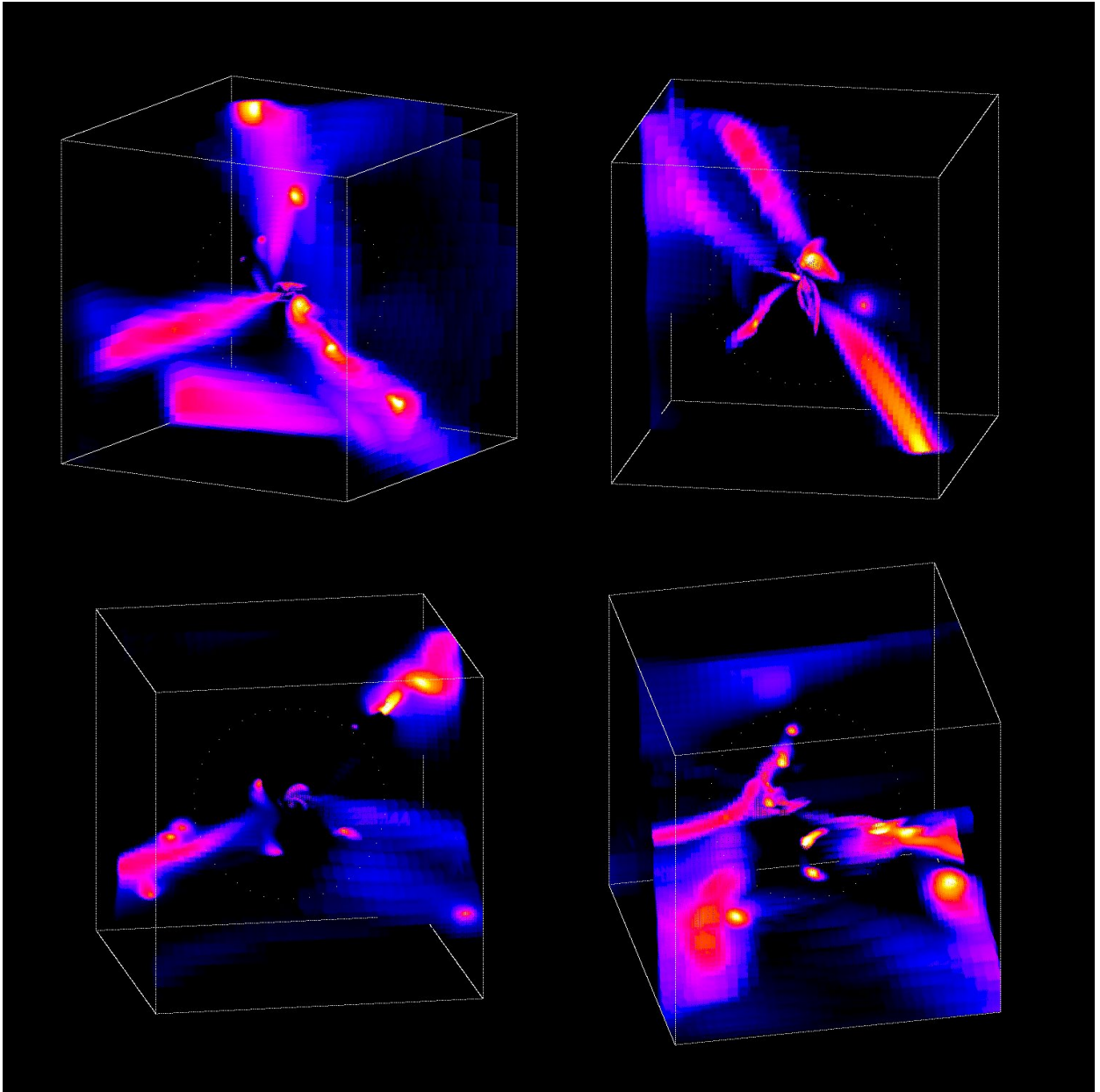


Figure 10. Inward flux in the three-dimensional boxes of side 320 kpc centered on galaxies 314, 303, 311 and 310 from the MareNostrum simulations. The colours refer to inflow rate per solid angle of point-like tracers at the centers of cubic-grid cells. The dotted circle marks the virial radius. All haloes show high-flux streams, some smooth and some with embedded clumps. Galaxy 310 (bottom right) is undergoing multiple minor mergers due to the particularly clumpy streams.

5 Accretion profiles and probability distribution

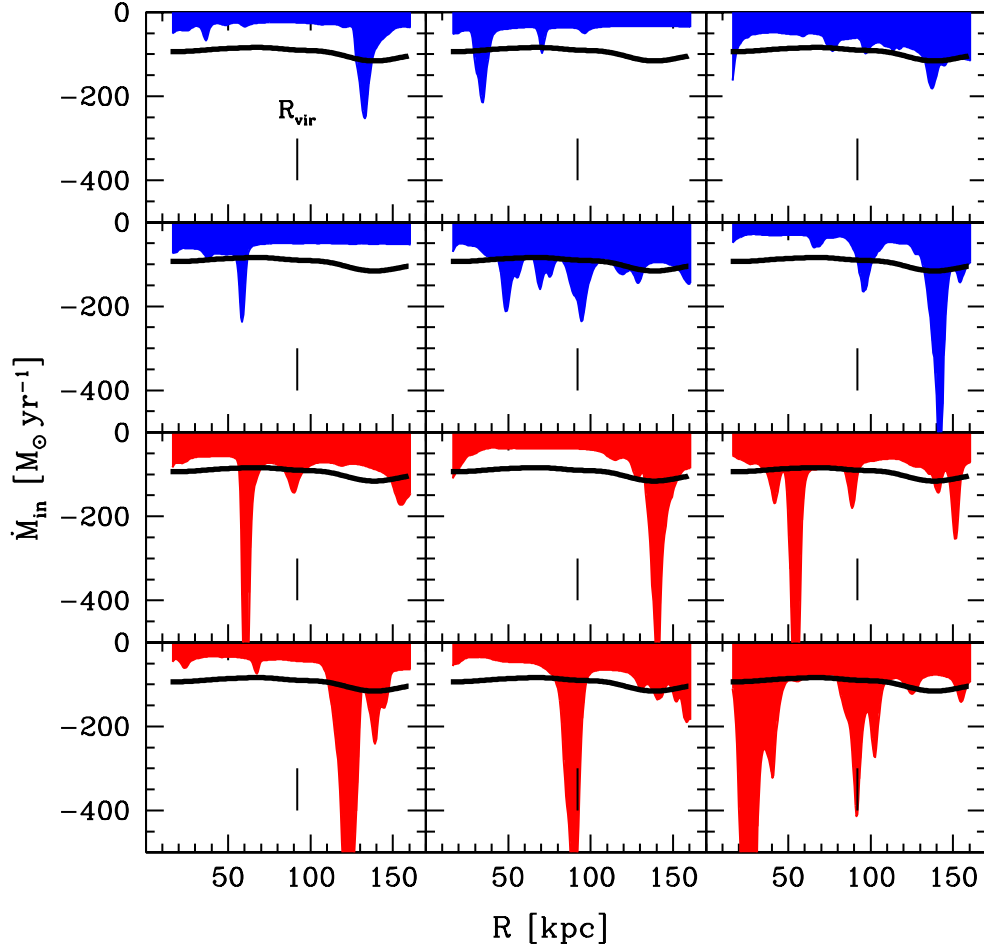


Figure 11. Profiles of total gas inflow rate through spherical shells as in Fig. 3 of the Letter. Shown here are twelve galaxies of $M_v \simeq 10^{12} M_\odot$ at $z = 2.5$, randomly chosen from the simulation. The lower six panels show clumps that correspond to mergers of mass ratio $\mu > 0.1$, while the upper six are fed by smoother flows with only mini-minor mergers of $\mu < 0.1$.

Fig. 11 is an extension of Fig. 3 of the Letter, presenting the influx profiles of twelve galaxies, all with $M_v \simeq 10^{12} M_\odot$ at $z = 2.5$, chosen at random from the MareNostrum simulation. The profiles extend from $r = 15$ kpc, the disk vicinity, to $r = 160$ kpc, almost twice the virial radius of $R_v \simeq 90$ kpc.

In order to evaluate the conditional probability $P(\dot{M}|M_v)$ that enters Eq. 2 of the Letter, we first measure $P_0(\dot{M}|M_0)$ from a fair sample of MareNostrum haloes of our fiducial case $M_0 = 10^{12} M_\odot$ at $z_0 = 2.5$. This probability distribution, shown in Fig. 12, is derived by sampling the $\dot{M}(r)$ profiles shown in Fig. 11 uniformly in r , using the fact that the inflow velocity along the streams is roughly constant. The tail of the distribution shown in Fig. 12, at $\dot{M} > 200 M_\odot \text{yr}^{-1}$, is dominated by $\mu > 0.1$ mergers, while the main body

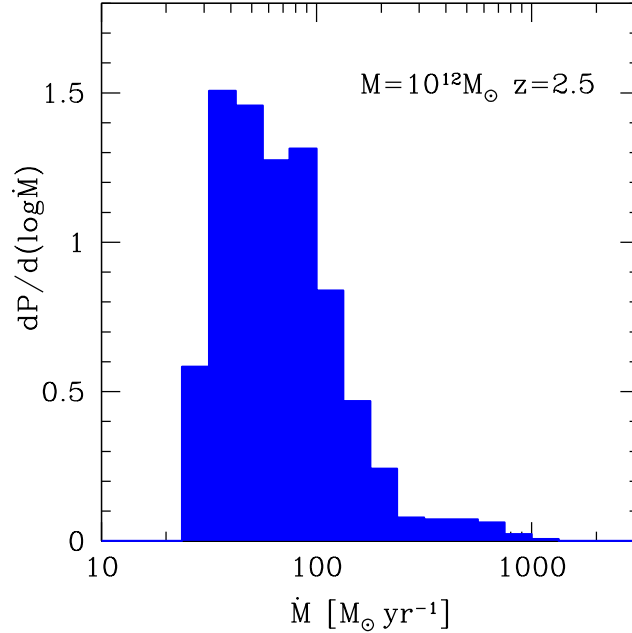


Figure 12. The conditional probability distribution $P(\dot{M}|M_v)$ for the fiducial case $M_v = M_0 = 10^{12} M_\odot$ at $z = 2.5$.

of the distribution is mostly due to smoother streams. Recall that the average is about $100 M_\odot \text{yr}^{-1}$.

We then generalize $P_0(\dot{M}|M_0)$ to other masses M_v using the scaling from eq. (4), $\dot{M} \propto M_v^{1.15}$, namely

$$P(\dot{M}|M_v) = P_0[\dot{M}(M_0/M_v)^{1.15}|M_0] . \quad (7)$$

At $z \sim 2.5$, this scaling of \dot{M} is good to within a factor of two for $M_v \leq 10^{13} M_\odot$, beyond which it becomes a more severe overestimate (Goerdt et al., in preparation). The results for other redshifts ($z > 2$) are obtained using the scaling from eq. (4), $\dot{M} \propto (1+z)^{2.25}$.

Half the galaxies shown in Fig. 11 turn out to show clumps leading to mergers of $\mu > 0.1$, and the rest show only smaller clumps in smoother flows. One can read from the relative width of the clumps in Fig. 11 that the duty cycle for $\mu > 0.1$ clumps in each individual galaxy is less than 0.1. By comparing the areas above the individual profiles with the average for galaxies of that mass and redshift, one can see that on average only about one third of the stream mass is in clumps.

A similar estimate is obtained from EPS, by reading from Fig. 6 of Neistein & Dekel⁷ the rate $dN/d\omega$ of $> \mu$ mergers into a halo M_v . The typical starburst duration is $\Delta t \simeq 0.1 R_v/V_v$ (~ 50 Myr at $z = 2.5$), based on merger simulations²⁹ or the typical peak width in the $\dot{M}(r)$ profiles (Fig. 11), given streaming at the virial velocity $V_v = (GM_v/R_v)^{1/2} \sim 220 \text{ km s}^{-1}$. This leads to $\eta = (dN/d\omega)\Delta t \simeq 0.09$ for $M = 2 \times 10^{12} M_\odot$ at $z = 2.2$.

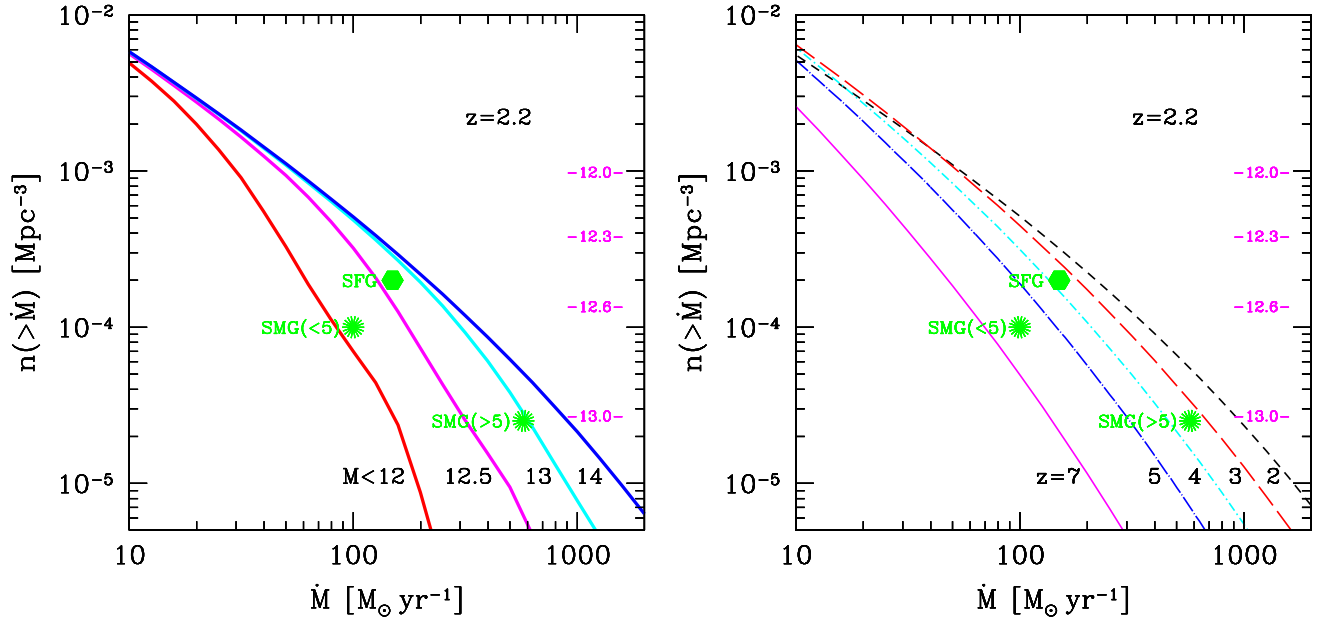


Figure 13. Comoving number density of galaxies with total gas inflow rate higher than \dot{M} at $z = 2.2$, as in Fig. 4 of the main body of the Letter. The numbers in magenta next to the right axis refer to $\log M_v$ of haloes with the corresponding abundance. **Left:** Dependence on the maximum halo mass that contributes to cold streams, for $M_{\text{stream}} = 10^{12}, 10^{12.5}, 10^{13}, 10^{14} M_\odot$. **Right:** Variation with redshift, $z = 2, 3, 4, 5, 7$.

6 The abundance as a function of mass and redshift

As described above, the conditional probability distribution $P(\dot{M}|M_v)$ has been estimated by scaling the results from the simulated haloes of $M_v = 10^{12} M_\odot$. Preliminary analysis of more massive haloes at that redshift (T. Goerdt et al., in preparation) indicates that the actual inflow rate starts dropping below the adopted estimate in haloes more massive than $M_{\text{stream}} \sim 10^{13} M_\odot$. For a first crude estimate of the effect this might have on our results shown in Fig. 4 of the Letter, we re-compute the comoving number density $n(>\dot{M})$ as described in the main text, but now limit the halo mass range that contributes to \dot{M} by an upper cutoff at M_{stream} . Fig. 13 shows the results for different values of M_{stream} . We see that a cutoff at $M_{\text{stream}} = 10^{13} M_\odot$ makes only a small difference to $n(>\dot{M})$, by a factor of ~ 2 at the high- \dot{M} regime corresponding to the bright SMGs. Thus, the decay of cold streams above $10^{13} M_\odot$ is not expected to alter our results in a qualitative way. On the other hand, we learn from the fact that the symbols for SFGs and bright SMGs lie far above the lower curve that the high-SFR objects at these redshifts are dominated by central galaxies in haloes more massive than $10^{12} M_\odot$. In fact, we read from the figure that some of the SFGs and many of the bright SMGs are associated with haloes more massive than $3 \times 10^{12} M_\odot$.

Fig. 13 also shows the predicted abundance $n(>\dot{M})$ at different redshifts, now applying no finite upper mass cutoff M_{stream} . This is justified for $z > 2$ based on our preliminary

investigation of the MareNostrum galaxies at different redshifts and masses and consistent with the conjecture of DB06⁸ shown in Fig. 5. We see that the comoving abundance of galaxies with $\dot{M} \sim 150 M_{\odot} \text{yr}^{-1}$ is predicted to vary by a factor less than two between $z=2$ and 4. By $z \sim 7$ that abundance drops by an order of magnitude. The variation with redshift is somewhat larger at the high-flux end, toward $\dot{M} \sim 10^3 M_{\odot} \text{yr}^{-1}$. At lower redshifts, the contribution of streams in massive haloes above M_{shock} is most likely overestimated by this procedure, so a similar analysis in the low- z regime should impose an upper limit at $M_{\text{stream}} \simeq M_{\text{shock}}$.